RSC Advances

PAPER

View Article Online
View Journal | View Issue

Cite this: *RSC Adv.*, 2020, **10**, 4763

The synthesis of a $BiOCl_xBr_{1-x}$ nanostructure photocatalyst with high surface area for the enhanced visible-light photocatalytic reduction of Cr(VI)†

Muhammad Bilal Hussain, * Malik Saddam Khan, Herman Maloko Loussala and Muhammad Sohail Bashir

The photocatalytic reduction of poisonous Cr(VI) to environmentally friendly Cr(III) driven by visible-light is highly foreseen. The construction of heterojunctions is a promising and solid strategy to tune the photocatalytic performance of BiOCl in the visible region. Herein, for the first time, we report Cr(VI) reduction by a $BiOCl_{0.8}Br_{0.2}$ composite produced *via* a facile *in situ* synthetic process at room temperature while making use of PVP (MW = 10 000). In this study, a series of $BiOCl_xBr_{1-x}$ nanocomposites with different concentrations of chlorine and bromine have been prepared. The results show that $BiOCl_{0.8}Br_{0.2}$ has crystalline lattice, a large surface area (147 m^2 g^{-1}), a microporous structure (0.377 cm^3 g^{-1}), and very high chemical stability. It is revealed that the $BiOCl_{0.8}Br_{0.2}$ composite is much more active than those synthesized using different molar concentrations of chlorine and bromine. The DRS analysis and high photocurrent suggested that $BiOCl_{0.8}Br_{0.2}$ possessed absorption properties under visible light, which is beneficial for the efficient generation and separation of electron–hole pairs. In addition, we evaluated the photocatalytic activity of $BiOCl_{0.8}Br_{0.2}$ on the reduction of Cr(VI) under visible light irradiation and found that the obtained composite material exhibited a higher photocatalytic activity than single BiOCl or BiOBr without any decline in the activity after five cycles and is the best performing photocatalyst among those tested.

Received 6th December 2019
Accepted 13th January 2020

DOI: 10.1039/c9ra10256f

rsc.li/rsc-advances

1. Introduction

Photocatalysis is an environmentally friendly and cost-effective approach to ease the serious anxieties of ecological deterioration due to substantial metals ascending from manufacturing wastelands.[1,2] Among several toxic heavy metals, cancer-causing chromium Cr(VI) is a tarnished pollutant found in left-over water due to its solubility.[3] The reduction of Cr(VI) to Cr(III) by a semiconductor photocatalyst is a possible solution for waste-water treatment because of the intrinsic environmental friendliness of Cr(III).[4] Visible light occupies about 49% of sunlight energy and considerable efforts have been made to take full advantage of solar energy and to explore diverse, novel photocatalysts working under visible-light irradiation.[5]

For the easy photocatalytic degradation of organic contaminants and the reduction of heavy metal ions, bismuth oxyhalides, including BiOCl, are auspicious aspirants but their efficiency is not pleasing due to their inappropriate band gap value (E_g), valence band (VB) position, and conduction band (CB) position.[6] $BiOCl_xBr_{1-x}$ systems are responsive to visible-light and have tunable E_g values, VBs, and CBs. Due to the strong oxidation ability of $BiOCl_xBr_{1-x}$ systems, they seem to be attractive photocatalysts for the reduction of heavy metals and the degradation of organic pollutants.[7–10] However, strategies for the $BiOCl_xBr_{1-x}$ nanocomposite desorption and hole scavenging to remove Cr(VI) have not been successfully reported at room temperature.

As a traditional photocatalyst, BiOCl can be activated by UV irradiation ($\lambda < 390$ nm).[11] However, the efficiency of solar energy conversion is limited by its large band gap (3.2 eV).[12–14] To resolve this issue, many visible-light active photocatalysts, including BiOBr,[15] UiO-66-NH_2,[5] NH_2-MIIL-125(Ti),[16] MIL-88(B)-NH_2,[17] ZIF-67,[18] and $BiVO_4$,[19] have been well reported; however, their poor photocatalytic activities and slow photocatalytic reduction rates do not meet the required standards for large scale water treatments.[20] Therefore, the development of highly effective and stable visible light dynamic photocatalysts for the reduction of Cr(VI) is immediately needed.[6,20] So far, composite photocatalysts are more photocatalytically active than single photocatalysts, as the

Key Laboratory of Interfacial Reaction & Sensing Analysis in University of Shandong, School of Chemistry and Chemical Engineering, University of Jinan, Jinan 250022, Shandong, P. R. China. E-mail: bilal.fcc288794@qq.com

† Electronic supplementary information (ESI) available. See DOI: 10.1039/c9ra10256f

composites reduce recombination and enhance the separation of electron–hole pairs.[1,21] Hence, work should be done to boost the efficiency of composite photocatalysts. Numerous new visible light-driven photocatalysts have been developed, among which BiOBr is one of the most promising candidates. BiOBr has an indirect narrow band gap of 2.80 eV and a layered structure with interlaced, positively charged $[Bi_2O_2]^{2+}$ slabs and negatively charged double [Br] slices,[22–24] enabling it not only to absorb visible light but also to separate photogenerated carriers using an internal electric field.[25] However, the photocatalytic activity of BiOBr is still not efficient enough for practical applications.[19]

To further improve the photocatalytic efficiency, BiOBr has been coupled with other semiconductors either to extend the light absorption range or to increase the separation efficiency of the photoinduced carriers. Some BiOBr-based composites have been reported including BiOBr/g-C_3N_4,[26,27] BiOBr/CeO_2,[28] Bi_2MoO_6/BiOBr,[29] Bi_2WO_6/BiOBr,[30] CdS/BiOBr,[31] BiOBr/BiOI,[32] and BiOCl/Bi_2S_3.[33] Recently, BiOBr was coupled with low cost, chemically stable BiOCl and improved photocatalytic performances were achieved.[7,19,34] Nevertheless, a facile design of high-quality $BiOCl_{0.8}Br_{0.2}$ nanocomposites with satisfactory photocatalytic performance for the reduction of Cr(VI) *via* an easy synthetic process is still a challenging problem. It is thermodynamically possible for MnO_2 to oxidize Cr(III) under aerobic and slightly anoxic conditions. According to literature, trivalent chromium Cr(III) can be easily converted into hexavalent chromium in the temperature range of 200–300 °C, and the conversion rate can reach 50% in 12 hours.[35] Therefore, in order to overcome this serious problem, some room temperature synthetic materials such as $BiOCl_{0.8}Br_{0.2}$ nanocomposites are urgently needed to successfully reduce Cr(VI) to Cr(III).

Herein, a $BiOCl_{0.8}Br_{0.2}$ photocatalyst was synthesized *via* a facile *in situ* synthetic process for the first time with PVP (MW = 10 000) at room temperature for the reduction of Cr(VI) under visible light. The growth of the composite typically increases the surface area to a great extent and effectively promotes electron transfer and separation. The as-prepared $BiOCl_{0.8}Br_{0.2}$ photocatalyst shows considerable photocatalytic activity and can reduce Cr(VI) under visible light irradiation. Finally, a possible mechanism for the improved photocatalytic activity of the $BiOCl_{0.8}Br_{0.2}$ composite is proposed in light of the experimental results.

1.1 Materials and physical measurements

All chemicals and reagents used for the synthesis and analysis were used as received without further purification. Ethylene glycol (EG, 99.9%) and ethanol (C_2H_5OH, 99.9%) were all of reagent-grade and purchased from Xilong Chemical Industry Incorporated Co. Ltd. Polyvinylpyrrolidone PVP (MW = 10 000), was obtained from Sigma-Aldrich. Bismuth nitrate pentahydrate ($Bi(NO_3)_3 \cdot 5H_2O$, 99%), diphenylcarbazide (DPC, 98%), and potassium dichromate ($K_2Cr_2O_7$, 99.8%) were purchased from Shanghai Macklin Biochemical Co. Ltd. Sodium chloride (NaCl, 99.9%), sodium bromide (NaBr, 99.9%), and sodium sulfate (Na_2SO_4, 99.9%) were purchased from Sinopharm Chemical Reagents Co. Ltd. The indium-doped tin oxide (ITO) glass substrates were obtained from China Southern Glass Co., Ltd., Shenzhen, China and were then well cleaned *via* ultrasonication in deionized water and absolute ethanol for 15 min sequentially. Deionized water was prepared using a Milli-Q water purification system (18.25 MΩ cm).

1.2 Preparation of the $BiOCl_{0.8}Br_{0.2}$-NP composite

Typically, 4 mL of 0.25 M $Bi(NO_3)_3 \cdot 5H_2O$ in EG was ultrasonically injected into a 50 mL plastic centrifuge tube, which contained EG and water, under vigorous magnetic stirring. Subsequently, 0.1 mL of a 1 M PVP (MW = 10 000, 0.1 mL, 1 M) solution was added dropwise into the above colorless solution. After stirring for 5 min, aqueous solutions of NaCl (0.3 mL, 3 M) and NaBr (0.3 mL, 3 M) were introduced together at a rate of 0.2 mL min^{-1} and then were continuously stirred for 2 min till the formation of a uniform milk-white colloid solution. The final volume ratio of water to EG in the reaction mixture solution was 1 : 1 and the concentrations of PVP, $Bi(NO_3)_3$, and NaCl were 25, 25, and 225 mM, respectively. Finally, the system was statically kept on an experiment table under ambient conditions for two hours. The light-yellow products were gradually deposited on the bottom of the centrifuge tube and the supernatant solution became clear after 1 h. Then, the product was facilely collected by discarding the upper solution and washed repeatedly for characterization and performance studies. The obtained sample was washed several times using de-ionized water and ethanol for the complete exclusion of the undesired water-soluble products. The obtained solid compound was subsequently dried at 60 °C overnight in an electric oven under normal atmospheric conditions. For assessment purposes, pure BiOCl and BiOBr were also prepared separately under the same circumstances.

1.3 Characterization

The products were characterized *via* transmission electron microscopy (TEM, JEM-1400, energy dispersive). X-ray diffraction (XRD) spectra were recorded on a Bruker D8 Focus X-ray diffractometer with Cu Kα radiation (λ = 0.15418 nm) by depositing the sample on an amorphous silicon substrate. Nitrogen (N_2) adsorption–desorption isotherms were recorded on a Micromeritics TriStar II 3020 instrument at 77 K. Before measurements, the samples were degassed and dried at 200 °C under vacuum for 4 h. The specific surface area was calculated according to the Brunauer–Emmett–Teller (BET) method. Fourier transform infrared spectroscopy (FTIR) was conducted on a PerkinElmer VERTEX 70 FTIR spectrophotometer. The diffuse reflectance spectra (DRS) of the BiOCl samples were measured using a UV-vis-NIR spectrophotometer (Shimadzu UV-3101PC) in the wavelength range of 200 to 600 nm (a PerkinElmer). Photoluminescence (PL) spectra and PL lifetimes were recorded on an Edinburgh FLS920 Multifunction Steady State and Transient State Fluorimeter.

1.4 Photoelectrochemical measurements

Photoelectrochemical measurements were performed on a Solartron Analytical electrochemical analyzer (ModuLab XM) in a standard three-electrode system by utilizing a Pt foil as the counter electrode and Ag/AgCl (KCl, 3 M) as the reference electrode. The working electrodes were prepared by spreading ethanol dispersed slurries of the samples (10 mg in a 0.1 mL ethanol) onto the well-cleaned ITO glass substrates. Subsequently, the sample-coated substrates were dried in air for 10 min and then annealed at 80 °C for 5 min for the electrochemical impedance spectroscopy (EIS) analysis and photocurrent tests. For the photoelectrochemical measurements, all three electrodes were placed in a quartz cell containing a 0.5 M Na_2SO_4 aqueous solution as the electrolyte, which was bubbled by N_2 thoroughly to remove oxygen before the measurement. The transient photocurrent responses were recorded at a bias potential of 0.6 V under a 60 s on/off chopped illumination. The distance between the xenon lamp and the working electrode was about 2 cm. The EIS analysis was performed by using an alternating current voltage amplitude of 10 mV within the frequency range of 4 MHz to 100 MHz.

1.5 Photocatalytic activity measurements

Typically, a specific amount (20 mg) of the $BiOCl_xBr_{1-x}$ photocatalyst was dissolved in a 40 mL Cr(VI) solution (8 mg L^{-1}) and irradiated with visible light from a 300 W xenon lamp fitted with a 420 nm cut-off filter. The concentration of chromium in the reaction solution was determined *via* the DPC method and the reduction was performed at 30 °C. First, a 0.2 mL sample solution was taken after the photocatalytic reduction of Cr(VI) and mixed with H_2SO_4 (1.8 mL, 0.2 M) in a 2 mL tube. The freshly prepared DPC (0.40 μL, 0.25% (w/v)) in acetone was added to the tube. The mixture was shaken for about one minute and allowed to stand for 10 minutes to ensure that the color developed completely. Using deionized water as a reference, a red-violet to purple color change was observed. The photocatalytic efficiency was determined by dividing C/C_0, where C is the remaining Cr(VI) concentration and C_0 is the starting Cr(VI) concentration. Furthermore, the stability and repeatability of the as-synthesized $BiOCl_xBr_{1-x}$ composites were investigated by the photocatalytic reduction of Cr(VI). In this study, $BiOCl_xBr_{1-x}$ was recycled for seven times in the same photocatalytic reaction. After each cycle, the catalyst was separated from the suspension by centrifugation at (8000 rpm). Finally, the photocatalyst was collected by centrifugation (8000 rpm), washed with deionized water and ethanol, dried overnight under vacuum at 60 °C, and continuously circulated.

2. Results and discussions

The XRD patterns of the $BiOCl_{0.8}Br_{0.2}$ composites with different chlorine to bromine ratios are shown in Fig. 2a. Clearly, all the catalysts are highly crystallized. BiOCl (JCPDS 06-0249) and BiOBr (JCPDS 85-0682)[36] have tetragonal structures and high purity because no other specific diffraction peak was detected. The observation is in agreement with that in the literature. The $BiOCl_{0.8}Br_{0.2}$ composite shows the same result. The diffraction peaks of the $BiOCl_{0.8}Br_{0.2}$ composite displays a two-phase substance containing BiOCl and BiOBr. Upon the addition of BiOBr, the characteristic peaks of BiOCl were weakened in the diffraction patterns of the $BiOCl_{0.8}Br_{0.2}$ composite. This result was caused by the fact that BiOBr particles inhibited the crystal growth of BiOCl.

The morphology of the as-prepared samples was examined *via* transmission electron microscopy. Fig. 1 shows a typical TEM image of a $BiOCl_{0.8}Br_{0.2}$ sample. Similarly, the TEM images of BiOCl and BiOBr are displayed separately in Fig. S1.† It can be clearly realized that a flower-like $BiOCl_{0.8}Br_{0.2}$ tetragonal composite is present with an average diameter of 100–150 nm. The entire porous flower-like $BiOCl_{0.8}Br_{0.2}$ microspheres are self-assembled by numerous BiOCl/Br nanosheets. The final product was optimized and their corresponding TEM images are shown in Fig. S2–S7.†

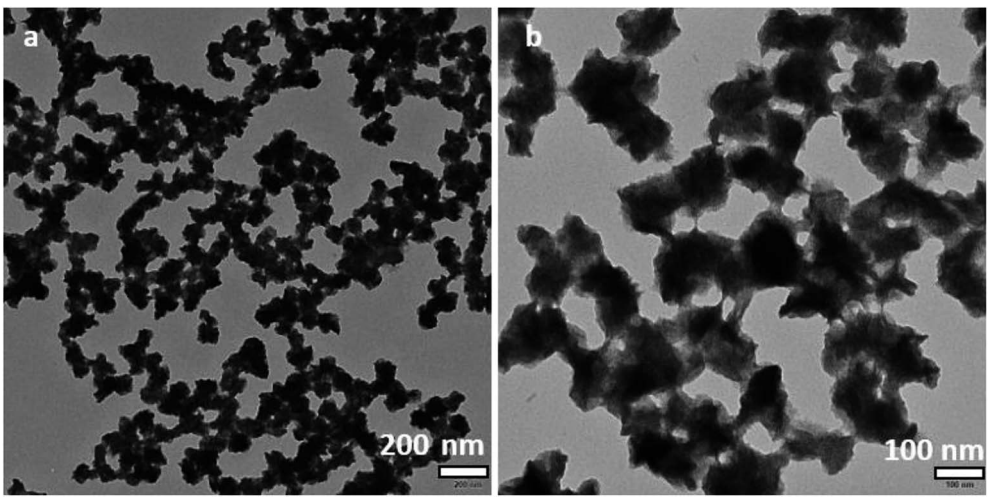

Fig. 1 (a) Low-and (b) high-magnification TEM images of $BiOCl_{0.8}Br_{0.2}$-NPs.

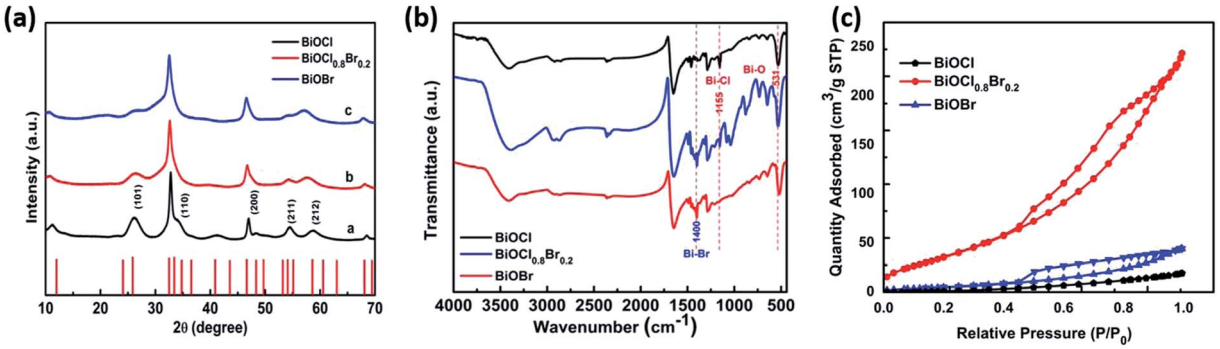

Fig. 2 (a) The powder X-ray diffraction (PXRD) pattern, (b) FTIR spectra, and (c) nitrogen adsorption–desorption isotherms at 77 K for pure BiOCl, BiOBr and the $BiOCl_{0.8}Br_{0.2}$-NPs.

FTIR was successfully used to investigate the functional groups in the as-synthesized sample. The FTIR spectra of BiOCl, BiOBr, and the $BiOCl_{0.8}Br_{0.2}$ composite are presented in Fig. 2b. The curve of pristine BiOCl and BiOBr has a representative absorption band at 531 cm^{-1}, which was assigned to the Bi–O stretching mode and indicates the existence of Bi–O bonds in BiOCl, BiOBr and the $BiOCl_{0.8}Br_{0.2}$ composite, respectively. Moreover, the small absorption band at 1155 cm^{-1} and 1400 cm^{-1} is probably due to the symmetric vibrational stretch of Bi–Cl and Bi–Br bonds present in BiOCl or BiOBr and its presence can be visualized in the $BiOCl_xBr_{1-x}$ composites, which indicate the existence of Bi–Cl and Bi–Br in the heterostructure. The above results reveal that BiOCl and BiOBr have been coupled together in the $BiOCl_{0.8}Br_{0.2}$-NPs.

The adsorption–desorption isotherms of BiOCl, BiOBr and the $BiOCl_{0.8}Br_{0.2}$-NP composite are shown in Fig. 2c. The BET surface areas of BiOCl and BiOBr were 22 $m^2\ g^{-1}$ and 25 $m^2\ g^{-1}$, respectively. After successfully synthesizing the $BiOCl_{0.8}Br_{0.2}$-NP composite, the BET surface area increased to 147 $m^2\ g^{-1}$. It is expected that the greater specific surface area of the photocatalyst will supply more surface-active sites and make charge carrier transport easier, leading to an enhanced photocatalytic performance.

2.1 Photocatalytic activity

The photocatalytic activities of the as-prepared samples were assessed using the photocatalytic reduction of aqueous Cr(VI) under visible light (λ > 420 nm). Before irradiation, the suspensions were magnetically stirred in dark for 30 minutes to establish the absorption–desorption equilibrium. The concentration of Cr(VI) did not significantly change throughout the process in the absence of a photocatalyst. This showed that aqueous Cr(VI) does not spontaneously undergo photolytic reduction under visible light irradiation and that photocatalysts play a vital role in the reduction of aqueous Cr(VI). Moreover, all of the $BiOCl_xBr_{1-x}$-NP composites exhibited higher photocatalytic activity when compared with pure BiOCl or BiOBr under the same conditions. Fig. 3a also shows that the $BiOCl_{0.8}Br_{0.2}$ composite had higher Cr(VI) reduction rates than pure BiOCl and BiOBr. The enhanced photocatalytic activity of the $BiOCl_{0.8}Br_{0.2}$ composites can be partly attributed to the strong adsorption of Cr(VI) molecules. In Fig. 3b, we can see that the absorption peak intensity of Cr(VI) at 540 nm gradually decreased with the increase in the irradiation time. After irradiation for 20 min, the characteristic absorption peak intensity fell to almost zero, indicating that the heavy metal pollutant Cr(VI) had been fully reduced. Moreover, the catalytic activity of the $BiOCl_{0.8}Br_{0.2}$ composite can be well-maintained after several

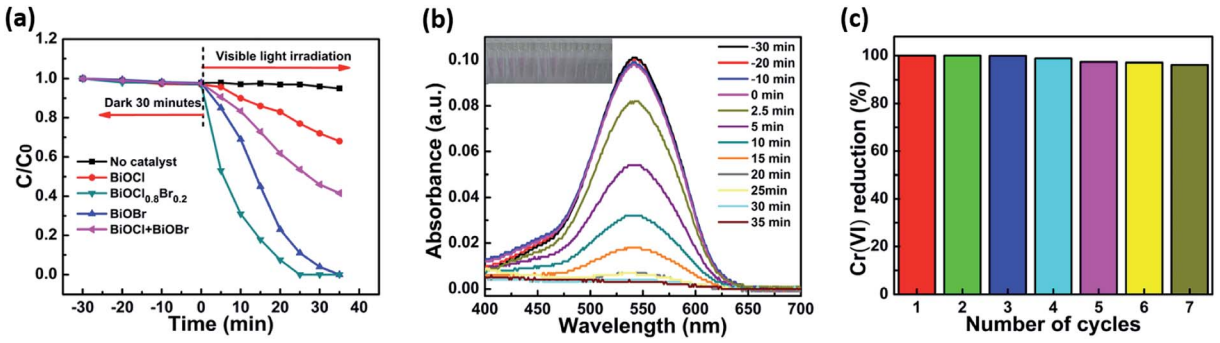

Fig. 3 (a) Photocatalytic activities of BiOCl, BiOB, and $BiOCl_{0.8}Br_{0.2}$-NP composite in the reduction of aqueous Cr(VI) under visible light (λ > 420 nm) irradiation. (b) Cr(VI) reduction efficiencies of $BiOCl_{0.2}Br_{0.2}$-NPs. (c) The multi-cycle reduction results of Cr(VI) with $BiOCl_{0.8}Br_{0.2}$-NPs. The reaction conditions were 20 mg of photocatalyst, 40 mL of 8 mg L^{-1} Cr(VI) solution, a reaction temperature of 30 °C and a pH value of ≈2.

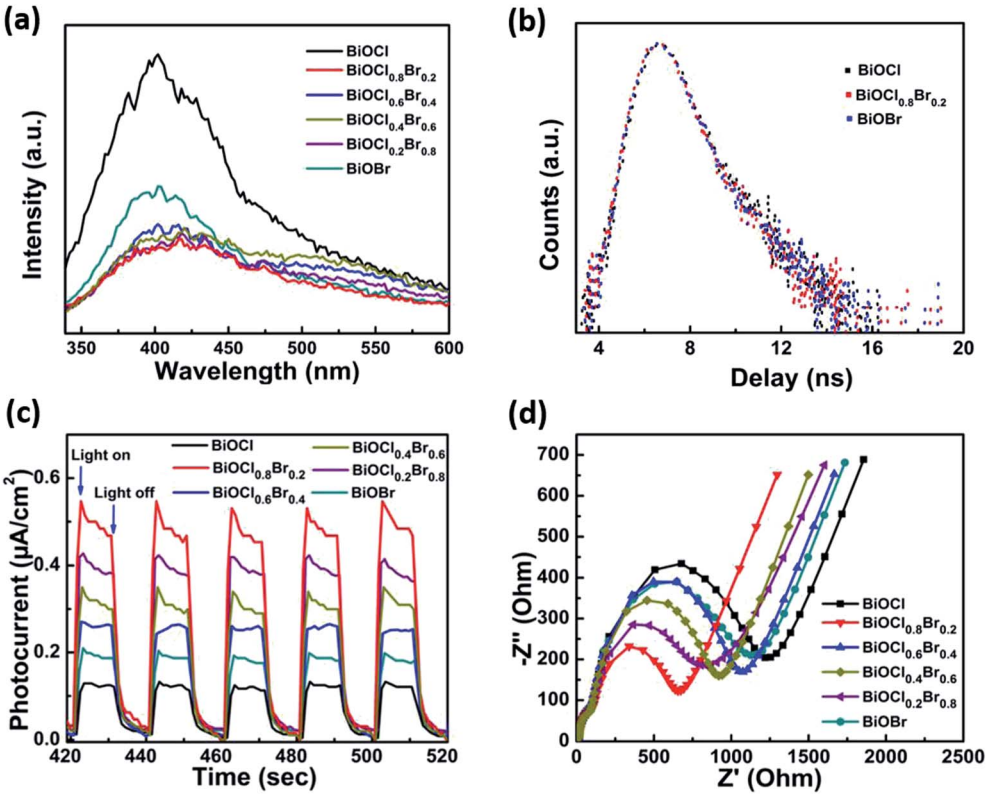

Fig. 4 (a) Photoluminescence (PL) spectra, (b) spectra of time-resolved transient photoluminescence parameters (TRPL), (c) transient photocurrent response (TPR) curves, and (d) electrochemical impedance (EIS) spectra of BiOCl, BiOBr, and the various composites.

reduction cycles (Fig. 3d) and more interestingly no obvious decline in performance was observed.

The photoluminescence emission spectra (PL) were recorded to systemically investigate the mechanism of separation and recombination of the photogenerated electron–hole pairs. As displayed in Fig. 4a, the PL intensity of the $BiOCl_{0.8}Br_{0.2}$-NPs is lower than that of pure BiOCl and BiOBr, which indicates the recombination of the photogenerated electrons and holes. Therefore, the results of the photocurrent responses and PL studies demonstrate that the heterostructure between BiOCl and BiOBr can effectively suppress the recombination of the photogenerated electrons and holes, and thus enhance the corresponding photocatalytic reduction of aqueous Cr(VI).[19,36,37]

The recombination and separation of the photogenerated electrons and holes could be further investigated by time-resolved transient PL (TRPL), as shown in Fig. 4b. The TRPL parameters of bare BiOCl, $BiOCl_{0.8}Br_{0.2}$, and BiOBr are shown in Table 1. Interestingly, the average lifetime (τ_a) of bare BiOCl and BiOBr is prolonged after the formation of the $BiOCl_{0.8}Br_{0.2}$ composite.[38] The increased average lifetime further indicates that the recombination of the photogenerated charge carriers is suppressed. These PL results are in accordance with the photoelectrochemical measurements. To investigate the interfacial charge separation efficiency, the photocurrent responses of BiOCl, BiOBr, $BiOCl_{0.2}Br_{0.8}$, $BiOCl_{0.2}Br_{0.8}$, $BiOCl_{0.6}$, and $Br_{0.4}BiOCl_{0.8}Br_{0.2}$ were measured under identical experimental conditions. As can be seen from Fig. 4c, the order of the photocurrent response intensity is $BiOCl_{0.8}Br_{0.2}$ > $BiOCl_{0.2}Br_{0.8}$ > $BiOCl_{0.4}Br_{0.8}$ > $BiOCl_{0.6}Br_{0.4}$ > BiOBr > BiOCl, which is consistent with the results of the DRS mentioned above. The BiOCl sample shows the lowest photocurrent response, which can be attributed to the fast recombination of the photogenerated electron–hole pairs. Meanwhile, the photocurrent response of BiOBr is also relatively strong because of its small band gap. However, the photocurrent response of $BiOCl_{0.8}Br_{0.2}$ is much higher than that of pure BiOBr or BiOCl, indicating the greater ability of the composite to effectively separate and transfer charge under visible light irradiation.

To further confirm the above results, electrochemical impedance spectroscopy (EIS), a useful measurement to characterize charge carrier transportation, was also tested. As shown in Fig. 4d the $BiOCl_{0.8}Br_{0.2}$ composite exhibits a smaller impedance arc diameter, revealing lower charge transfer resistance in comparison to pure BiOCl or BiOBr.

Table 1 Time-resolved transient photoluminescence parameters (TRPL) of BiOCl $BiOCl_{0.8}Br_{0.2}$, and BiOBr

Sample	τ_1 (ps)	τ_2 (ns)	I_1 (%)	I_2 (%)
BiOCl	163.7	1.259	78.78	21.32
$BiOCl_{0.8}Br_{0.2}$	313.9	1.363	88.54	11.16
BiOBr	241.7	1.382	81.28	18.72

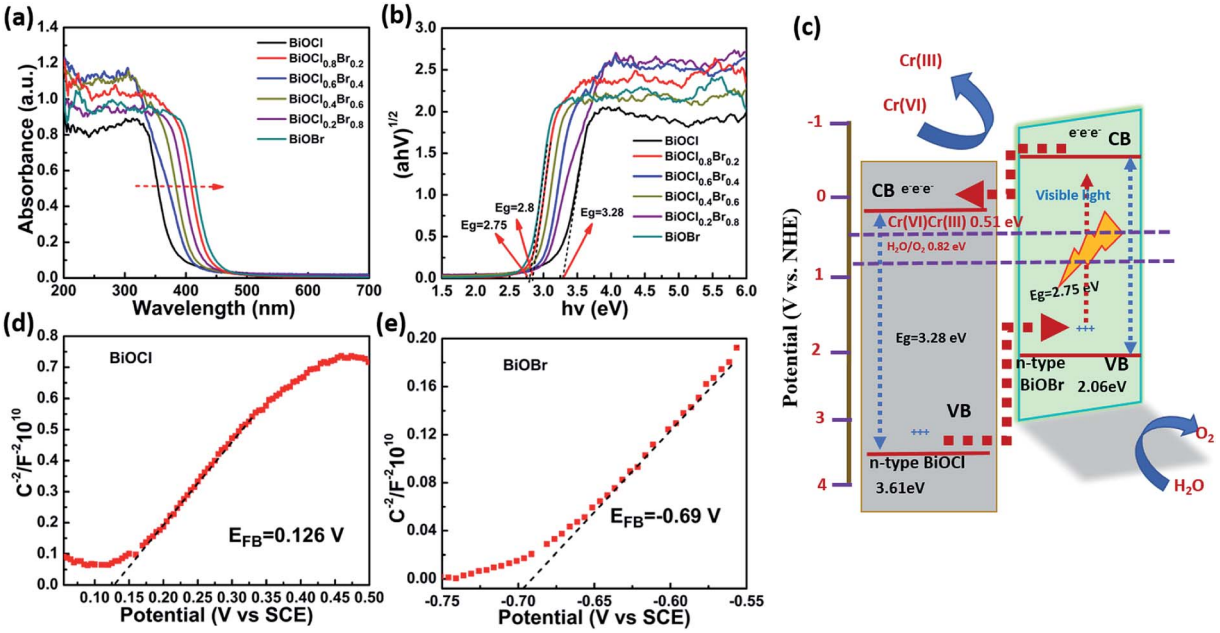

Fig. 5 (a) UV-vis diffuse reflectance spectra (DRS) and (b) band-gap values assessed by a correlated curve of $(ah\nu)^{1/2}$ set against photon energy plots of the as-synthesized $BiOCl_xBr_{1-x}$ NPs. (c) Energy level alignment scheme, derived from the results obtained from individual components, for the $BiOCl_{0.8}Br_{0.2}$-NPs. Schottky plots of (d) BiOCl and (e) the BiOBr-NPs.

The optical absorption properties of pure BiOCl, BiOBr, and the $BiOCl_{0.8}Br_{0.2}$ composite were examined *via* UV-vis absorption spectroscopy, and the spectra are presented in Fig. 5a and b. After the growth of the $BiOCl_{0.8}Br_{0.2}$-NP composite, the absorption edge of the $BiOCl_{0.8}Br_{0.2}$ composite displayed a slight blue-shift in comparison to pure BiOBr. This may be an effect of the heterostructure of BiOBr. However, when compared with bare BiOCl, an apparent red-shift in the DRS of the $BiOCl_{0.8}Br_{0.2}$-NP composite was observed. This red-shift may indicate that the composite absorbs visible light more strongly in comparison to bare BiOCl. According to a previous study, the band gaps (E_g) of the above samples can be obtained from plotting $(ah\nu)^{1/2}$ (eV $cm^{-1})^2$ *versus* photon energy ($h\nu$). The band gaps of BiOCl and BiOBr are estimated as 3.28 eV and 2.8 eV, respectively. Meanwhile, the E_g value of $BiOCl_{0.8}Br_{0.2}$-NPs is estimated to be 2.75 eV. Subsequently, this result implies that the $BiOCl_{0.8}Br_{0.2}$-NP composite can use the full spectrum of visible light to generate photoelectrons and holes because of its appropriate band gap.

To define the energy level alignment of the as-prepared BiOCl and BiOBr systems, capacity measurements were performed to determine their flat band potential. Fig. 5d and e show the resulting Mott–Schottky plots for BiOCl and BiOBr. The CBs values are found to be 0.126 V and −0.69 V for BiOCl and BiOBr, respectively.[33,39] Correspondingly, the VB values for BiOCl and BiOBr are calculated to be 3.61 and 2.06 eV according to their band gap energy (E_g) values. The values determined in this study are similar to those reported in previous literature. Moreover, the slope of the BiOCl and BiOBr samples are positive, implying that they are n-type semiconductors, which makes them promising photoanodes. Since the VB and CB potentials of BiOBr are both more negative than those of BiOCl and their reduction potential is more negative than the Cr(VI)/Cr(III) potential (0.51 V, pH ≈ 2), the mechanism of Cr(VI) reduction using the $BiOCl_{0.8}Br_{0.2}$ composite can be explained from the scheme presented in Fig. 5c. When the composite is exposed to visible light irradiation, both the BiOCl and BiOBr components are excited and produce photogenerated electrons (e^-) and holes (h^+). Simultaneously, the e^- from BiOBr can rapidly transfer to the CB of BiOCl, while the h^+ from BiOCl can migrate to the VB of the BiOBr. Therefore, the photogenerated electrons and holes are separated efficiently and their recombination is retarded in the photocatalytic $BiOCl_{0.8}Br_{0.2}$ composite, leading to greater photocatalytic activity as compared to pure BiOCl and BiOBr. Finally, $Cr_2O_7^{2-}$ is reduced to Cr(III) by the photogenerated electrons and $^{\bullet}O_2^-$ is produced by the reduction of O_2.

To increase our understanding of the reaction, some basic technical measurements were performed during the reduction of Cr(VI) to find photoactive species. To attain this, $AgNO_3$, citric acid, and benzoquinone (BQ) were used as e^-, h^+, and $^{\bullet}O_2^-$ scavengers, respectively.[40] After ten minutes of light irradiation, the reduction ratio of various hole scavengers including $AgNO_3$, benzoquinone (BQ), and citric acid are 69.6%, 33.2%, and 27.2%, respectively (Fig. 6a). The reduction ratio is about 2.6, 1.51 times smaller and 1.37 times greater compared to no hole scavenger whose reduction efficiency is (50.49%) as displayed in (Fig. 6b). Interestingly, the addition of $AgNO_3$ as an electron trap strongly delays the reduction of Cr(VI), which indicates that the electrons in the reaction system play a vital role.[41] In addition, since there was a significant enhancement in the photocatalytic reduction when citric acid was added to trap h^+, it can be

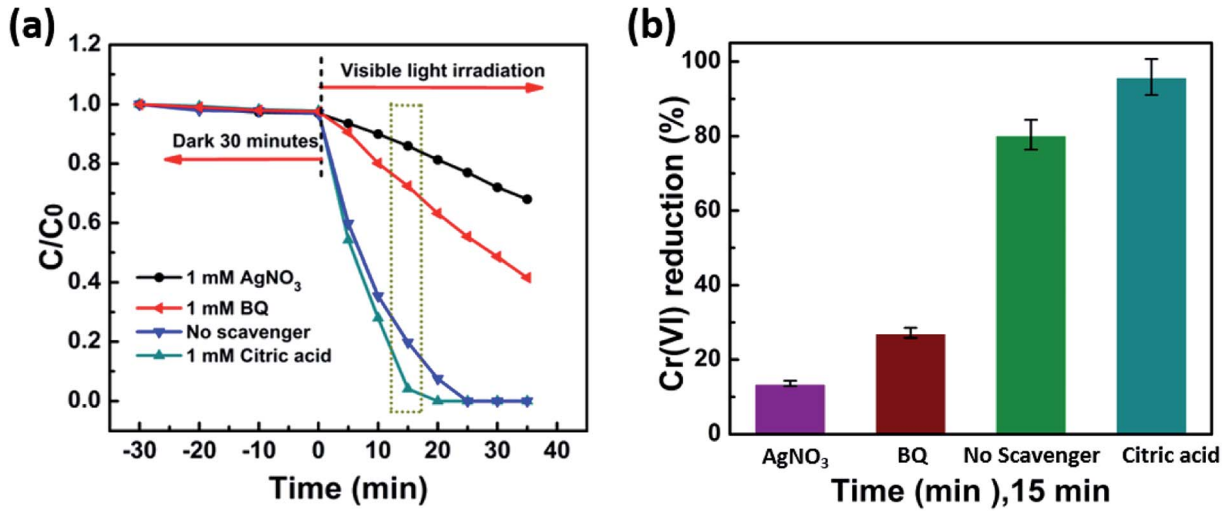

Fig. 6 (a) Trapping experiment of the active species for Cr(VI) reduction in the presence of $BiOCl_{0.8}Br_{0.2}$-NP composite under visible light irradiation. (b) Comparison of the Cr(VI) reduction efficiencies over $BiOCl_{0.8}Br_{0.2}$ in the presence of 1 mM $AgNO_3$, 1 mM BQ, no scavenger and 1 mM citric acid respectively.

concluded that citric acid was capable of capturing the holes generated after excitation.[42] Thus, as the h^+ ions are captured by citric acid, following recombination the extra electrons could be used for the reduction of Cr(VI). The reduction of Cr(VI) declined distinctly after the addition of 1 mM BQ, which indicates the involvement of the $^{\bullet}O_2^-$ radical in reaction media.[33,43] Electrons play a significant role in Cr(VI) reduction and similarly, it is also affected by $^{\bullet}O_2^-$ to some extent. From the details discussion above, a reasonable mechanism for the reduction of Cr(VI) using the newly synthesized composites in the presence of visible light irradiation was proposed. Charge transporters, photogenerated electrons and holes that are generated following visible light radiation, move quickly on the surface of the catalyst. Almost all of the electrons react with oxygen to form $^{\bullet}O_2^-$, which is involved in the reduction process while some of the electrons can directly reduce Cr(VI). Hence $^{\bullet}O_2^-$ radicals play key role in Cr(VI) reduction.

$$BiOCl_{0.8}Br_{0.2} + h\nu \rightarrow e^- + h^+ \quad (1)$$

$$Cr_2O_7^{2-} + H^+ + e^- \rightarrow Cr^{3+} + H_2O \quad (2)$$

$$e^- + O_2 \rightarrow {}^{\bullet}O_2^- \quad (3)$$

3. Conclusion

In summary, a series of $BiOCl_xBr_{1-x}$ composites were effectively synthesized *via* a new facile method with an attractive morphology for applications as visible light photocatalysts for the efficient reduction of Cr(VI). The results proved that a mixture of glycol and water in a 1 : 1 ratio was the optimum solvent and room temperature was the optimum temperature for the synthesis of the aforementioned composites. Other factors including the concentration of bismuth and PVP were also optimized. Furthermore, the band gap could be controlled by changing the ratio of chlorine and bromine in the $BiOCl_{0.8}Br_{0.2}$ solutions. The 3D hierarchical flower-like $BiOCl_{0.8}Br_{0.2}$ microspheres have a comparatively super-high surface area, this resulted in a highly efficient visible-light photocatalyst. In addition, the features of this morphology and the greater specific surface area improved the light-harvesting properties of the composite, and thus boosted the active catalytic sites, charge separation and migration of $BiOCl_{0.8}Br_{0.2}$ into solid solutions. Moreover, the recombination of the photogenerated electrons and holes was largely suppressed. The photocatalytic activity of $BiOCl_{0.8}Br_{0.2}$ reached a maximum at this ratio and decreased as the concentration of bromine decreased for all other samples. The catalyst also showed excellent stability and sustained efficiency even after five cycles of Cr(VI) reduction. This work could open new possibilities to provide some insight into the synthesis of photocatalysts with controllable structures, high surface areas, optimal bandgap engineering, and photoelectric properties for a range of applications.

Conflicts of interest

There are no conflicts of interests to declare.

References

1 G. Zhang, D. Chen, N. Li, Q. Xu, H. Li, J. He and J. Lu, Preparation of $ZnIn_2S_4$ nanosheet-coated CdS nanorod heterostructures for efficient photocatalytic reduction of Cr(VI), *Appl. Catal., B*, 2018, **232**, 164–174.
2 Y. C. Zhang, L. Yao, G. Zhang, D. D. Dionysiou, J. Li and X. Du, One-step hydrothermal synthesis of high-performance visible-light-driven SnS_2/SnO_2 nanoheterojunction photocatalyst for the reduction of aqueous Cr(VI), *Appl. Catal., B*, 2014, **144**, 730–738.

3 X.-S. Wang, C.-H. Chen, F. Ichihara, M. Oshikiri, J. Liang, L. Li, Y. Li, H. Song, S. Wang, T. Zhang, Y.-B. Huang, R. Cao and J. Ye, Integration of adsorption and photosensitivity capabilities into a cationic multivariate metal-organic framework for enhanced visible-light photoreduction reaction, *Appl. Catal., B*, 2019, **253**, 323–330.

4 Y. C. Zhang, J. Li and H. Y. Xu, One-step in situ solvothermal synthesis of SnS_2/TiO_2 nanocomposites with high performance in visible light-driven photocatalytic reduction of aqueous Cr(VI), *Appl. Catal., B*, 2012, **123–124**, 18–26.

5 L. Shen, S. Liang, W. Wu, R. Liang and L. Wu, Multifunctional NH_2-mediated zirconium metal-organic framework as an efficient visible-light-driven photocatalyst for selective oxidation of alcohols and reduction of aqueous Cr(VI), *Dalton Trans.*, 2013, **42**, 13649–13657.

6 F. Deng, Y. Luo, H. Li, B. Xia, X. Luo, S. Luo and D. D. Dionysiou, Efficient toxicity elimination of aqueous Cr(VI) by positively-charged $BiOCl_xI_{1-x}$, $BiOBr_xI_{1-x}$ and $BiOCl_xBr_{1-x}$ solid solution with internal hole-scavenging capacity via the synergy of adsorption and photocatalytic reduction, *J. Hazard. Mater.*, 2020, **383**, 121127.

7 X. Jia, J. Cao, H. Lin, M. Zhang, X. Guo and S. Chen, Transforming type-I to type-II heterostructure photocatalyst via energy band engineering: a case study of I-BiOCl/I-BiOBr, *Appl. Catal., B*, 2017, **204**, 505–514.

8 D. Ma, H. Liu, J. Huang, J. Zhong, J. Li and D. Wang, Improved photocatalytic performance of flower-like BiOBr/BiOCl heterojunctions prepared by an ionic liquid assisted one-step hydrothermal method, *Mater. Lett.*, 2019, **238**, 147–150.

9 X. Chang, M. A. Gondal, A. A. Al-Saadi, M. A. Ali, H. Shen, Q. Zhou, J. Zhang, M. Du, Y. Liu and G. Ji, Photodegradation of Rhodamine B over unexcited semiconductor compounds of BiOCl and BiOBr, *J. Colloid Interface Sci.*, 2012, **377**, 291–298.

10 M. Guan, C. Xiao, J. Zhang, S. Fan, R. An, Q. Cheng, J. Xie, M. Zhou, B. Ye and Y. Xie, Vacancy associates promoting solar-driven photocatalytic activity of ultrathin bismuth oxychloride nanosheets, *J. Am. Chem. Soc.*, 2013, **135**, 10411–10417.

11 Z. Liu, H. Ran, B. Wu, P. Feng and Y. Zhu, Synthesis and characterization of BiOI/BiOBr heterostructure films with enhanced visible light photocatalytic activity, *Colloids Surf., A*, 2014, **452**, 109–114.

12 L. Lin, M. Huang, L. Long, Z. Sun, W. Zheng and D. Chen, Fabrication of a three-dimensional BiOBr/BiOI photocatalyst with enhanced visible light photocatalytic performance, *Ceram. Int.*, 2014, **40**, 11493–11501.

13 M. Pelaez, N. T. Nolan, S. C. Pillai, M. K. Seery, P. Falaras, A. G. Kontos, P. S. M. Dunlop, J. W. J. Hamilton, J. A. Byrne, K. O'Shea, M. H. Entezari and D. D. Dionysiou, A review on the visible light active titanium dioxide photocatalysts for environmental applications, *Appl. Catal., B*, 2012, **125**, 331–349.

14 A. M. Ganose, M. Cuff, K. T. Butler, A. Walsh and D. O. Scanlon, Interplay of Orbital and Relativistic Effects in Bismuth Oxyhalides: BiOF, BiOCl, BiOBr, and BiOI, *Chem. Mater.*, 2016, **28**, 1980–1984.

15 Z. Fan, Y. Zhao, W. Zhai, L. Qiu, H. Li and M. R. Hoffmann, Facet-dependent performance of BiOBr for photocatalytic reduction of Cr(VI), *RSC Adv.*, 2016, **6**, 2028–2031.

16 H. Wang, X. Yuan, Y. Wu, G. Zeng, X. Chen, L. Leng, Z. Wu, L. Jiang and H. Li, Facile synthesis of amino-functionalized titanium metal-organic frameworks and their superior visible-light photocatalytic activity for Cr(VI) reduction, *J. Hazard. Mater.*, 2015, **286**, 187–194.

17 L. Shi, T. Wang, H. Zhang, K. Chang, X. Meng, H. Liu and J. Ye, An Amine-Functionalized Iron(III) Metal-Organic Framework as Efficient Visible-Light Photocatalyst for Cr(VI) Reduction, *Adv. Sci.*, 2015, **2**, 1500006.

18 X. Li, X. Gao, L. Ai and J. Jiang, Mechanistic insight into the interaction and adsorption of Cr(VI) with zeolitic imidazolate framework-67 microcrystals from aqueous solution, *Chem. Eng. J.*, 2015, **274**, 238–246.

19 J. Zhang, J. Lv, K. Dai, C. Liang and Q. Liu, One-step growth of nanosheet-assembled BiOCl/BiOBr microspheres for highly efficient visible photocatalytic performance, *Appl. Surf. Sci.*, 2018, **430**, 639–646.

20 J. Shang, W. Hao, X. Lv, T. Wang, X. Wang, Y. Du, S. Dou, T. Xie, D. Wang and J. Wang, Bismuth Oxybromide with Reasonable Photocatalytic Reduction Activity under Visible Light, *ACS Catal.*, 2014, **4**, 954–961.

21 H. Gnayem and Y. Sasson, Nanostructured 3D Sunflower-like Bismuth Doped $BiOCl_xBr_{1-x}$ Solid Solutions with Enhanced Visible Light Photocatalytic Activity as a Remarkably Efficient Technology for Water Purification, *J. Phys. Chem. C*, 2015, **119**, 19201–19209.

22 Z. Cui, H. Song, S. Ge, W. He and Y. Liu, Fabrication of BiOCl/BiOBr hybrid nanosheets with enhanced superoxide radical dominating visible light driven photocatalytic activity, *Appl. Surf. Sci.*, 2019, **467–468**, 505–513.

23 J. C. Sin, C. A. Lim and S. M. Lam, Photocatalytic degradation of organic pollutants using surfactant-free hydrothermally prepared flower-like BiOBr hierarchical structures under visible light irradiation, *IOP Conf. Ser. Earth Environ. Sci.*, 2018, **151**, 012022.

24 X. Zhang, L. W. Wang, C.-Y. Wang, W.-K. Wang, Y.-L. Chen, Y.-X. Huang, W.-W. Li, Y.-J. Feng and H.-Q. Yu, Synthesis of $BiOCl_xBr_{1-x}$ Nanoplate Solid Solutions as a Robust Photocatalyst with Tunable Band Structure, *Chem.–Eur. J.*, 2015, **21**, 11872–11877.

25 R. He, D. Xu, B. Cheng, J. Yu and W. Ho, Review on nanoscale Bi-based photocatalysts, *Nanoscale Horiz.*, 2018, **3**, 464–504.

26 L. Ye, J. Liu, Z. Jiang, T. Peng and L. Zan, Facets coupling of BiOBr-g-C_3N_4 composite photocatalyst for enhanced visible-light-driven photocatalytic activity, *Appl. Catal., B*, 2013, **142–143**, 1–7.

27 S.-R. Zhu, Q. Qi, Y. Fang, W.-N. Zhao, M.-K. Wu and L. Han, Covalent Triazine Framework Modified BiOBr Nanoflake with Enhanced Photocatalytic Activity for Antibiotic Removal, *Cryst. Growth Des.*, 2017, **18**, 883–891.

28 S. Zhang and D. Wang, Preparation of novel BiOBr/CeO_2 heterostructured photocatalysts and their enhanced photocatalytic activity, *RSC Adv.*, 2015, **5**, 93032–93040.

29 Y. Su, Z. Zhang, H. Liu and Y. Wang, $Cd_{0.2}Zn_{0.8}S$@UiO-66-NH_2 nanocomposites as efficient and stable visible-light-driven photocatalyst for H_2 evolution and CO_2 reduction, *Appl. Catal., B*, 2017, **200**, 448–457.

30 J. Xia, J. Di, S. Yin, H. Xu, J. Zhang, Y. Xu, L. Xu, H. Li and M. Ji, Facile fabrication of the visible-light-driven Bi_2WO_6/BiOBr composite with enhanced photocatalytic activity, *RSC Adv.*, 2014, **4**, 82–90.

31 W. Cui, W. An, L. Liu, J. Hu and Y. Liang, Synthesis of CdS/BiOBr composite and its enhanced photocatalytic degradation for Rhodamine B, *Appl. Surf. Sci.*, 2014, **319**, 298–305.

32 H. Huang, X. Han, X. Li, S. Wang, P. K. Chu and Y. Zhang, Fabrication of Multiple Heterojunctions with Tunable Visible-Light-Active Photocatalytic Reactivity in BiOBr–BiOI Full-Range Composites Based on Microstructure Modulation and Band Structures, *ACS Appl. Mater. Interfaces*, 2015, **7**, 482–492.

33 Q. Wang, W. Wang, L. Zhong, D. Liu, X. Cao and F. Cui, Oxygen vacancy-rich 2D/2D BiOCl-g-C_3N_4 ultrathin heterostructure nanosheets for enhanced visible-light-driven photocatalytic activity in environmental remediation, *Appl. Catal., B*, 2018, **220**, 290–302.

34 S. Zhang and J. Yang, Microwave-Assisted Synthesis of BiOCl/BiOBr Composites with Improved Visible-Light Photocatalytic Activity, *Ind. Eng. Chem. Res.*, 2015, **54**, 9913–9919.

35 A. D. Apte, V. Tare and P. Bose, Extent of oxidation of Cr(III) to Cr(VI) under various conditions pertaining to natural environment, *J. Hazard. Mater.*, 2006, **128**, 164–174.

36 J. Yang, Y. Liang, K. Li, Y. Zhu, S. Liu, R. Xu and W. Zhou, Design of 3D flowerlike $BiOCl_x$ Br_{1-x} nanostructure with high surface area for visible light photocatalytic activities, *J. Alloys Compd.*, 2017, **725**, 1144–1157.

37 L. Bai, F. Ye, L. Li, J. Lu, S. Zhong and S. Bai, Facet Engineered Interface Design of Plasmonic Metal and Cocatalyst on BiOCl Nanoplates for Enhanced Visible Photocatalytic Oxygen Evolution, *Small*, 2017, **13**, 1701607.

38 C. Xiao, M. Guan, J. Zhang, S. Fan, R. An, Q. Cheng, J. Xie, M. Zhou, B. Ye and Y. Xie, Vacancy Associates Promoting Solar-Driven Photocatalytic Activity of Ultrathin Bismuth Oxychloride Nanosheets, *J. Am. Chem. Soc.*, 2013, **135**, 10411–10417.

39 D. Wu, S. Yue, W. Wang, T. An, G. Li, H. Y. Yip, H. Zhao and P. K. Wong, Boron doped BiOBr nanosheets with enhanced photocatalytic inactivation of Escherichia coli, *Appl. Catal., B*, 2016, **192**, 35–45.

40 X. Tong, Z. Yang, J. Feng, Y. Li and H. Zhang, BiOCl/UiO-66 composite with enhanced performance for photo-assisted degradation of dye from water, *Appl. Organomet. Chem.*, 2018, **32**, e4049.

41 L. Shen, S. Liang, W. Wu, R. Liang and L. Wu, Multifunctional NH_2-mediated zirconium metal-organic framework as an efficient visible-light-driven photocatalyst for selective oxidation of alcohols and reduction of aqueous Cr(VI), *Dalton Trans.*, 2013, **42**, 13649–13657.

42 G. Zhang, D. Chen, N. Li, Q. Xu, H. Li, J. He and J. Lu, Preparation of $ZnIn_2S_4$ nanosheet-coated CdS nanorod heterostructures for efficient photocatalytic reduction of Cr(VI), *Appl. Catal., B*, 2018, **232**, 164–174.

43 L. Shen, W. Wu, R. Liang, R. Lin and L. Wu, Highly dispersed palladium nanoparticles anchored on UiO-66(NH_2) metal-organic framework as a reusable and dual functional visible-light-driven photocatalyst, *Nanoscale*, 2013, **5**, 9374–9382.